Shi *et al. Microstructures* **2025**, *5*, 2025081
DOI: 10.20517/microstructures.2024.194

Microstructures

Research Article

Open Access

A broadband self-powered and stable photothermoelectric detector based on Ag_2Se/MWCNTs composite fabricated via screen printing

Wei-Peng Shi, Rui Guo, Gai-Ling Tian, Yi Chen, Yong-Hua Wang, Dan-Feng Cui, Dan Liu, Chen-Yang Xue

State Key Laboratory of Extreme Environment Optoelectronic Dynamic Measurement Technology and Instrument, North University of China, Taiyuan 030051, Shanxi, China.

Correspondence to: Prof. Dan Liu, State Key Laboratory of Extreme Environment Optoelectronic Dynamic Measurement Technology and Instrument, North University of China, No.3 Xueyuan Road, Taiyuan 030051, Shanxi, China. E-mail: liudan235@nuc.edu.cn

How to cite this article: Shi, W. P.; Guo, R.; Tian, G. L.; Chen, Y.; Wang, Y. H.; Cui, D. F.; Liu, D.; Xue, C. Y. A broadband self-powered and stable photothermoelectric detector based on Ag_2Se/MWCNTs composite fabricated via screen printing. *Microstructures* **2025**, *5*, 2025081. https://dx.doi.org/10.20517/microstructures.2024.194

Received: 30 Dec 2024 **First Decision:** 4 Mar 2025 **Revised:** 15 Mar 2025 **Accepted:** 21 Mar 2025 **Published:** 8 Jul 2025

Academic Editors: Haijun Wu, Xiaozhou Liao **Copy Editor:** Xing-Yue Zhang **Production Editor:** Xing-Yue Zhang

Abstract

Photothermoelectric (PTE) detectors hold immense potential for converting incident light signals into electrical signals, finding applications in sensing, astronomy, night vision, and communication. However, their widespread adoption is hindered by issues such as slow response times, low responsivity, and poor stability. In this study, a high-performance self-powered PTE detector based on the Ag_2Se nanorods (NRs) and multi-walled carbon nanotubes (MWCNTs) is reported for the first time. The findings reveal that the electrical conductivity of the film increases with the addition of MWCNTs, albeit at the expense of the Seebeck coefficient. Notably, the film containing 0.5 wt% MWCNTs exhibited a superior power factor (303.22 $\mu W \cdot m^{-1} \cdot K^{-2}$) at 300 K. Owing to the high PTE performance, the photosensitive properties are characterized in an ultra-broadband range from the violet (405 nm) to infrared (2,500 nm) wavelengths, featuring rapid response time (1.4 s) and substantial output voltage (6.83 mV). Furthermore, the device demonstrated remarkable stability, with only a 3.4% decrease in output voltage after three months of air exposure and negligible changes in thirty cycles. Thus, the proposed device presents a novel strategy for developing PTE detectors characterized by broadband coverage, fast response times, and exceptional stability.

Keywords: Photothermoelectric detectors, broadband, screen printing, Ag_2Se, multi-walled carbon nanotubes

© The Author(s) 2025. **Open Access** This article is licensed under a Creative Commons Attribution 4.0 International License (https://creativecommons.org/licenses/by/4.0/), which permits unrestricted use, sharing, adaptation, distribution and reproduction in any medium or format, for any purpose, even commercially, as long as you give appropriate credit to the original author(s) and the source, provide a link to the Creative Commons license, and indicate if changes were made.

INTRODUCTION

High-performance photodetectors have a wide range of applications in communications, military surveillance, and environmental monitoring[1-3]. Most commercial ultraviolet or infrared photodetectors are made of wide or narrow bandgap semiconductor materials such as GaN, InGaAs, and HgCdTe. However, the bandgap of these photodetectors limits their broadband detection capability, and they face challenges such as high preparation costs and complex manufacturing processes[4,5]. To overcome these challenges, scientists have begun exploring alternative methods, with photothermoelectric (PTE) detectors emerging as a highly promising research direction.

Research on the PTE effect is crucial for energy conversion and optical sensing. Originating from the pursuit of efficient solar energy utilization, early investigations aimed to comprehend the fundamental mechanisms governing the interaction between light and thermoelectric (TE) materials[6-8]. It was uncovered that light interacting with TE materials induces a photothermal effect, raising local temperatures and generating a temperature gradient, thus resulting in the production of photothermal voltage via the Seebeck effect[9]. Over time, substantial advancements have been achieved in unraveling the intricacies of the PTE effect and its myriad applications, including photovoltaic energy harvesting[7,10-13], broadband measurements[8,14-18], and high-performance optical detection[8,15,19-23]. PTE photodetectors, distinguished by their self-powered capabilities and broadband response, have garnered significant attention[9]. However, despite promising prospects, challenges persist in optimizing the efficiency and stability of PTE devices across various operating conditions.

Unlike toxic Pb- or Te-based materials, Ag_2Se is chemically stable and non-leaching under operational conditions. Additionally, Ag_2Se exhibits an ultrahigh room-temperature ZT value (~1.2), enabling efficient heat-to-electricity conversion[24]. Recently, scientists have been actively exploring the possibility of applying Ag_2Se materials to PTE detection. For example, Yang et al. successfully enhanced the PTE conversion capability of Ag_2Se detectors by introducing a polypyrrole(PPy) light-trapping structure onto Ag_2Se thin films[25]. However, the current challenge lies in designing TE material structures that can fully utilize light energy. Although some vertical heterogeneous structures have made progress in photothermal conversion[11,26], there still exists an issue of insufficient utilization of light energy, resulting in wastage.

As is well known, carbon nanotubes (CNTs), with their high thermal conductivity[27,28], high electrical conductivity[29,30], and light absorption properties[31-33], have a wide range of applications in PTE detectors. Recent studies have shown that combining PPy[12], PEDOT:PSS[34], and MXene[35] is an effective way to enhance the PTE effect. However, these materials still have the disadvantages of low output voltage, long preheating time, and poor stability. This is due to the low Seebeck coefficient of carbon-based materials, which inherently limits their application in PTE detection. Nevertheless, the presence of π electrons makes the surface of CNTs highly chemically reactive, allowing interaction with TE materials. For example, hybrid materials such as Cu_2Se/MWCNTs[36], MoS_2/MWCNTs[37], SWCNTs/ZnO-NRs[38], SWCNTs/Ag_2Se[39], and MWCNTs/Ag_2Se[40,41] have shown improved TE properties compared to single constituents. Therefore, composite structures comprising CNTs and TE materials play a pivotal role in advancing TE technology.

In this study, Ag_2Se was blended with MWCNTs to enhance the TE properties and thus the PTE properties, and the TE and PTE performances were tested with different MWCNTs contents. The proposed Ag_2Se/polyvinyl pyrrolidone (PVP)/MWCNTs (APM) composite films exhibit excellent broadband voltage response and stable self-powered characteristics. Additionally, the mechanism behind the PTE effect was analyzed and explained by varying the conditions of laser power, wavelength, irradiation position, device length, and cycle time. After three months of exposure to air, the PTE voltage of the device decreased by

only 3.4%. Furthermore, the voltage output remained stable without any significant change over 30 cycles, demonstrating a high degree of stability. This study not only provides an environmentally friendly, inexpensive, and efficient method for preparing high-performance and reliable PTE devices but also offers a new approach to the design of PTE materials.

MATERIALS AND METHODS

Preparation of PTE detectors

Materials

Selenium dioxide (SeO_2), silver nitrate ($AgNO_3$), ethylene glycol (Eg), L-ascorbic acid, β-cyclodextrin, and terpineol were purchased from Shanghai Aladdin Biochemical Science and Technology Co., Ltd. PVP was purchased from Sinopharm Chemical Reagent Co., Ltd. MWCNTs was purchased from Kona New Materials Co., Ltd. All reagents can be used directly without purification.

Preparation of Ag_2Se/PVP/MWCNTs PTE thin film devices

Specific steps for the preparation of Ag_2Se nanorods (NRs) are given in the supporting information. Initially, the electrodes were prepared according to the position of the screen prints. Conductive silver paste was applied to the polyimide(PI) substrate and then heated and cured for 30 min at a constant temperature of 80 °C. Subsequently, 0.025 g of PVP was dissolved in 0.4 g of rosinol solution, and 0.5 g of Ag_2Se powder was dispersed in this solution. Different mass fractions of MWCNTs were added and manually milled until the mixture was smooth and fine. Mixed inks with MWCNT contents of 0, 0.25, 0.5, 0.75, 1, 1.5, and 2 wt% were prepared. These inks were screen-printed onto the PI substrate with Ag electrodes using a 200-mesh screen plate and then heated-cured at 80 °C under a nitrogen environment for 10 min to remove the terpineol alcohol. The screen printing and heat curing processes were repeated five times. Finally, silver wire was soldered on top of the conductive silver paste. The graphical pattern of the screen comprised five strips with sizes of 3 mm × 6 mm, 3 mm × 8 mm, 3 mm × 10 mm, 3 mm × 12 mm, and 3 mm × 14 mm. The specific process is illustrated in Supplementary Figure 1.

Characterization and measurement

Morphological and TE parameter acquisition

The surface morphology of the prepared Ag_2Se NRs films with different mass fractions of MWCNTs was investigated using field emission scanning electron microscopy (FESEM, SUPRA-55, ZEISS). The crystallinity and interplanar spacing of the samples were evaluated using a high-resolution transmission electron microscope (HRTEM) equipped with a 200 kV accelerating voltage (JSM2100F plus). The phase compositions of the APM were determined by X-ray diffraction (XRD, DX-2700). The Seebeck coefficient (S) and resistivity (σ) of the films were measured using a standard four-probe method (Linseis, LSR-3), with measurement errors of about ± 5%. The carrier concentration (n) and carrier mobility (μ) of the films were measured using the van der Pauw method (Linseis, HCS).

Optical parameter measurements

All output performance tests of the PTE were performed in a dark box. The current-voltage (I-V) curves under continuous laser irradiation were measured with a source meter (Keithley 2450), and the voltage-time (V-T) curves were collected by generating a pulsed laser using an electronic shutter (DHC GCI-73M). Lasers with eight different wavelengths (405, 650, 780, 808, 950, 1,550, 2,000, and 2,500 nm) were used during the measurements. The 1,550, 2,000, and 2,500 nm lasers were generated using a xenon lamp (MC-PF300) and a monochromator (7ISW301), and the optical power was determined using an optical power meter (MC-PM100D). The optical power was adjusted by varying the input voltage.

RESULTS AND DISCUSSION

XRD and surface morphology analysis

Figure 1A compares the X-ray diffraction (XRD) spectra of Ag_2Se and MWCNTs samples with different mass fractions. All samples are well indexed to β-Ag_2Se (PDF#24-1041), and no significant impurities are detected as the MWCNTs content increases. It is well known that the full width at half maximum (FWHM) of the XRD diffraction peaks is inversely proportional to the crystal size. To visually determine the crystallographic variations, the FWHM values corresponding to the strongest diffraction peaks of several samples are shown in Supplementary Table 1. The FWHM decreases with increasing MWCNT content, implying an increase in crystal size. However, the low structural dimension of MWCNTs results in low relative peak intensities, which are difficult to detect in the XRD pattern due to the much lower content of MWCNTs compared to Ag_2Se.

To confirm the presence of MWCNTs, SEM was used. SEM images of the surfaces with different mass fractions of MWCNTs (0, 0.5, 1, 1.5, and 2 wt%) are shown in Figure 1B-F. As seen in Figure 1B, the one-dimensional structure of Ag_2Se NRs grains remains relatively intact after screen printing. The adhesive effect of PVP leads to better binding of Ag_2Se on the PI substrate. In Figure 1C-F, the red circles indicate the positions of MWCNTs. The amount of MWCNTs in the images increases with the mass fraction. Figure 1G and H shows high-magnification SEM images and clearly reveals the distribution and dispersion of MWCNTs within the matrix, demonstrating their uniform dispersion and interfacial bonding with the surrounding material. To further elucidate the microstructure and the interaction between MWCNTs and the matrix, TEM analysis was performed. Figure 1I-L presents low- and high-resolution TEM (HRTEM) images of the 0.5 wt% APM film. In Figure 1I and J, the low-TEM images provide detailed insights into the morphology and distribution of MWCNTs at the nanoscale, confirming their homogeneous dispersion and alignment within the matrix. Figure 1L is the HRTEM image of the framed area in Figure 1K with the measured planar distances consistent with the (1 1 1) and (1 0 2) planes of Ag_2Se. Overall, these TEM and HRTEM images collectively demonstrate the well-dispersed MWCNTs and the crystalline structure of Ag_2Se within the APM film, highlighting the material's nanoscale characteristics and structural integrity.

TE properties of APM films

The electrical conductivity (σ), Seebeck coefficient (S), and power factor (PF) of five APM composite films (0, 0.25, 0.5, 0.75, and 1 wt%) were tested to investigate the change in TE properties of the composite films from 300 to 420 K.

Figure 2A shows the σ of the composite films. The σ of all films in Figure 2A increases with increasing temperature. For instance, the σ of the 0.5 wt% APM composite film increased from 249.76 $S\cdot cm^{-1}$ at 310 K to 259.86 $S\cdot cm^{-1}$ at 420 K. According to Equation (1):

$$\sigma = ne\mu \tag{1}$$

where σ is the electrical conductivity, n is the carrier concentration, and μ is the electron mobility. The σ of a semiconductor material is influenced by two factors: n and μ[42]. An increase in MWCNTs content leads to an increase in carrier concentration, as shown in Supplementary Figure 2A, while an increase in phonon scattering leads to a decrease in carrier mobility, as shown in Supplementary Figure 2B. In Ag_2Se-based materials, large amounts of Ag interstitial defects can result in n-type semiconducting behavior due to the electron-donating effect of interstitial Ag. Hence, the increased n should be mainly attributed to the observed additional interstitial Ag[39]. These factors compete, affecting the material's σ. At lower MWCNT content, the rise in carrier concentration has a more significant impact on σ than the decrease in mobility,

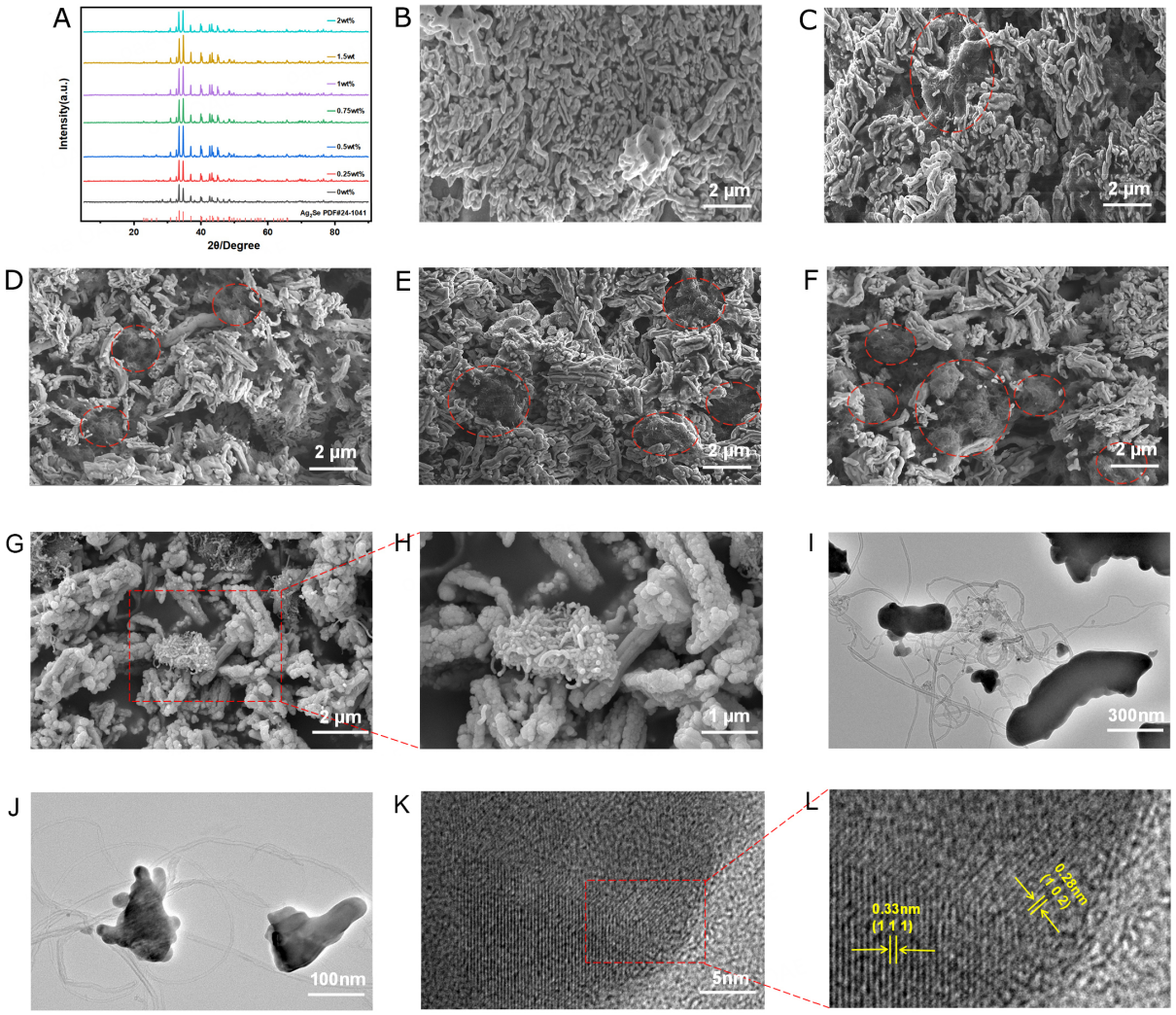

Figure 1. (A) XRD pattern of screen-printed 0-2 wt% APM films; SEM images when the contents of MWCNTs are (B) 0 wt%, (C) 0.5 wt%, (D) 1 wt%, (E) 1.5 wt%, and (F) 2 wt%; (G and H) High-magnification SEM images of the 0.5 wt% APM film; (I and J) Low- and (K and L) high-resolution HRTEM images of the 0.5 wt% APM film. XRD: X-ray diffraction; MWCNTs: multi-walled carbon nanotubes; APM: Ag_2Se/polyvinyl pyrrolidone/MWCNTs; SEM: scanning electron microscope; HRTEM: high-resolution transmission electron microscope.

resulting in increased σ as MWCNT content increases.

Figure 2B shows that the Seebeck coefficients of the films are all negative, consistent with Ag_2Se's n-type semiconductor nature. The Seebeck coefficients generally increase with temperature. For instance, the Seebeck coefficient of the 0.5 wt% APM composite film is -110.33 $\mu V \cdot K^{-1}$ at 300 K. However, when the temperature is increased from 400 to 420 K, the Seebeck coefficient decreases from -120.2 to -99.45 $\mu V \cdot K^{-1}$. Ag_2Se undergoes a phase transition from a low-temperature semiconducting phase to a high-temperature superconducting phase at around 407 K. The thermal conductivity was not measured in this experiment due to the small film thickness.

The TE properties of the flexible film depend on the PF, calculated using the Equation (2)[43]:

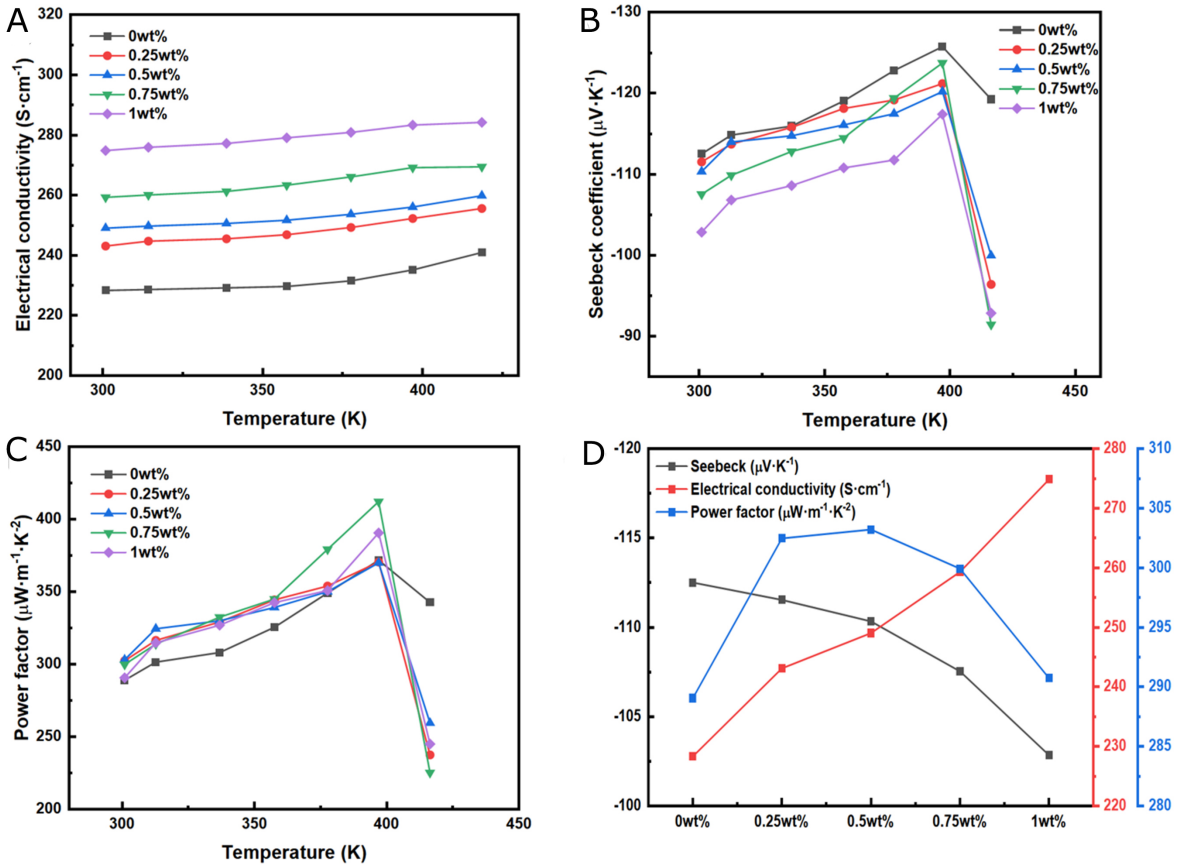

Figure 2. (A-C) Variation of σ, S, and PF with temperature for devices incorporating from 0 to 1 wt% MWCNTs; (D) Variation of σ, S, and PF with MWCNTs content at room temperature. σ: Electrical conductivity; S: Seebeck coefficient; PF: power factor; MWCNTs: multi-walled carbon nanotubes.

$$PF = S^2\sigma \tag{2}$$

where S is the Seebeck coefficient and σ is the electrical conductivity. The variation of the PF of the five films is shown in Figure 2C. Influenced by the σ and S, the PF of the 0.5 wt% MWCNTs is 303.22 $\mu W \cdot m^{-1} \cdot K^{-2}$ at 300 K, reaching a maximum value of 370.06 $\mu W \cdot m^{-1} \cdot K^{-2}$ at 400 K. When the temperature rises from 400 to 420 K, the PF decreases from 370.06 to 259.58 $\mu W \cdot m^{-1} \cdot K^{-2}$. The PF and Seebeck coefficients of different composite films exhibit similar patterns of change.

Since the PTE performance tests were all conducted at room temperature 300 K, only the TE performance with different contents of MWCNTs at 300 K is compared here, as shown in Figure 2D, the σ and S exhibit opposite trends with increasing MWCNT content. This occurs because MWCNTs increase the number of conductive channels in Ag_2Se NRs and improve its σ. However, MWCNTs also increase the carrier concentration of the device; it is known that the Seebeck coefficient varies inversely with the carrier concentration, resulting in a decrease. Therefore, the maximum PF of 303.22 $\mu W \cdot m^{-1} \cdot K^{-2}$ is only achieved at 0.5 wt%.

Test methods and optimal APM film selection

As illustrated in Figure 3A, the structure of Ag_2Se NRs has a trapped light effect that enhances light absorption when applied to the Ag bottom electrode. This is due to Ag's 90% ultra-high reflectivity in the

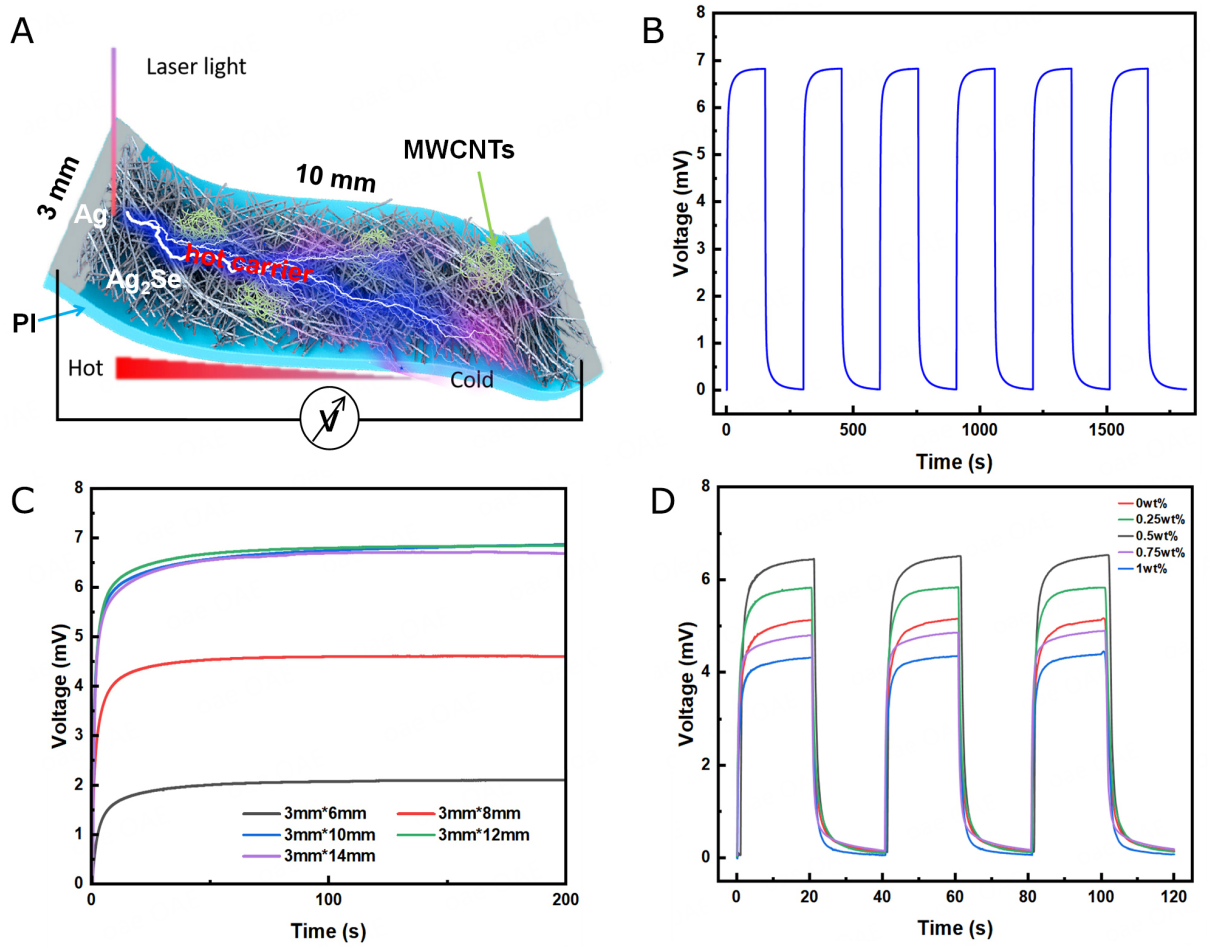

Figure 3. (A) Schematic of a PTE with Ag_2Se NRs and MWCNTs structures; (B) Time-resolved photoresponse. The wavelength was 650 nm with a power of 100 mW and the shutter opening and closing times are all 150 s; (C and D) Plots of output voltage as a function of device length and as a function of MWCNTs content; The wavelength was 650 nm with a power of 100 mW and (D) the shutter opening and closing times are all 20 s. PTE: Photothermoelectric; NRs: nanorods; MWCNTs: multi-walled carbon nanotubes.

UV to NIR region, which doubles the light path and increases absorption, resulting in greater photothermal conversion[19]. Additionally, different mass fractions of MWCNTs were added to the device. By adding varying fractions of MWCNTs, the TE ability of the device can be altered. The device absorbs photons on one side, creating a temperature difference with the other side. This drives the charge carriers to diffuse from the hot side to the cold side, and they move directionally with the temperature gradient, producing an electric field that leads to a stable output voltage.

To achieve a suitable switching time, multiple voltage switching tests were carried out, as shown in Figure 3B. The tests were performed under a 405 nm, 100 mW laser, using Ag_2Se thin film containing 0.5 wt% MWCNTs, in a 300 s cycle (with a shutter switching time of 150 s each). Due to the influence of thermal noise, the voltage in the 300 s cycle could not be reduced to 0. The PTE response increased from 24.44 μV to 6.83 mV, then decreased to 24.68 μV. The rise time (τ_{rise}) is 8.43 s and the fall time (τ_{fall}) is 9.27 s, as shown in Supplementary Figure 3, and remained stable for six cycles. As the rise and fall times were less than 150 s, a 40 s cycle (with a 20 s shutter switching time) was used for testing to ensure convenient measurement without affecting the results.

Since the 405 nm laser cannot be well controlled by regulating the input voltage to obtain a stable laser power density, and due to the potential harm to the human body from prolonged exposure to violet light, in the subsequent test, a 650 nm, 100 mW visible light was used to measure the PTE performance.

As shown in Figure 3C, the device length was varied from 6 to 14 mm to obtain the appropriate length for measurement. It was observed that under 650 nm, 100 mW laser irradiation, the output voltage initially increases with the length of the device. However, when the channel length exceeds 8 mm, the output voltage stabilizes at 6.83 mV with no further fluctuations. This indicates that the channel is long enough to prevent thermal diffusion from the hot end to the cold end. To conserve materials, the 3 mm × 10 mm sized device was used for subsequent performance testing.

In order to obtain the optimum APM film, the PTE output voltage of MWCNTs with different quality fractions was tested. The devices were irradiated with a 650 nm, 100 mW laser light source with a cycle period of 40 s. As illustrated in Figure 3D, the photovoltage initially increased with the mass fraction of MWCNTs, reaching a peak at 0.5 wt%, before subsequently declining. This may be due to the TE effect in combination with light absorption. Further photothermalelectrical performance measurements were carried out for MWCNTs content ranging from 0-3 wt%. The results indicated that the best performance was achieved at 0.5 wt%, as shown in Supplementary Figure 4. Unlike the conventional thermoelectric response, the photothermoelectric response depends not only on the Seebeck coefficient of the material itself, but also on the spectral absorption properties of the material itself. Additionally, it can be derived from Supplementary Figure 5 that in the optical wavelength range of 200-2,500 nm, the spectral absorption of the 0.5 wt% APM film is higher than that of the 0 wt% APM film. Therefore, the test concludes that the most desirable PTE characteristics are only present in the 0.5 wt% APM film. As a result, the 0.5 wt% APM film will be used for the subsequent performance tests.

Photothermoelectric mechanism and broadband response characteristics

The photovoltage generation in the APM device demonstrates clear PTE origin, as evidenced by the following experimental observations. First, the structural integrity of Ag_2Se remains preserved with limited PVP/MWCNT incorporation, as confirmed by maintained physical characteristics in Figure 4A. Spatially resolved measurements reveal position-dependent voltage polarity reversal under 1 mm-radius laser illumination, achieving maximum outputs of +6.37 mV and -5.84 mV at 2 mm and 9 mm positions, respectively, when fully illuminating the active surface. Systematic current-voltage characterization [Figure 4B and C] under varying laser powers (22.6-100 mW) shows progressive downward shifting of I-V curves from dark state to maximum illumination, with output voltages scaling within the -10 to 10 mV range. This power-dependent evolution aligns with the Seebeck effect principle[14], where enhanced photon-film interactions at higher intensities amplify thermal gradients, thereby strengthening the intrinsic electric field through carrier redistribution.

The wavelength-agnostic nature of the PTE mechanism fundamentally differs from bandgap-restricted optical processes. As demonstrated in Figure 4D, Ag_2Se nanorods exhibit broadband absorption spanning 405-2,500 nm, enabling efficient photon-to-thermal conversion across this spectral range. This wideband performance stems from the PTE's reliance on non-radiative relaxation processes rather than direct bandgap transitions. Supporting this interpretation, the linear photoresponse-power correlation in Figure 5A exhibits characteristic PTE behavior distinct from photovoltaic or bolometric mechanisms. Thermal characterization in Supplementary Figure 6 quantitatively confirms rapid surface heating dynamics under 650 nm irradiation (100 mW), recording a 50 °C temperature rise (20.3→70.3 °C) within 20 s. The temporally synchronized optoelectronic and thermal responses, monitored through simultaneous infrared

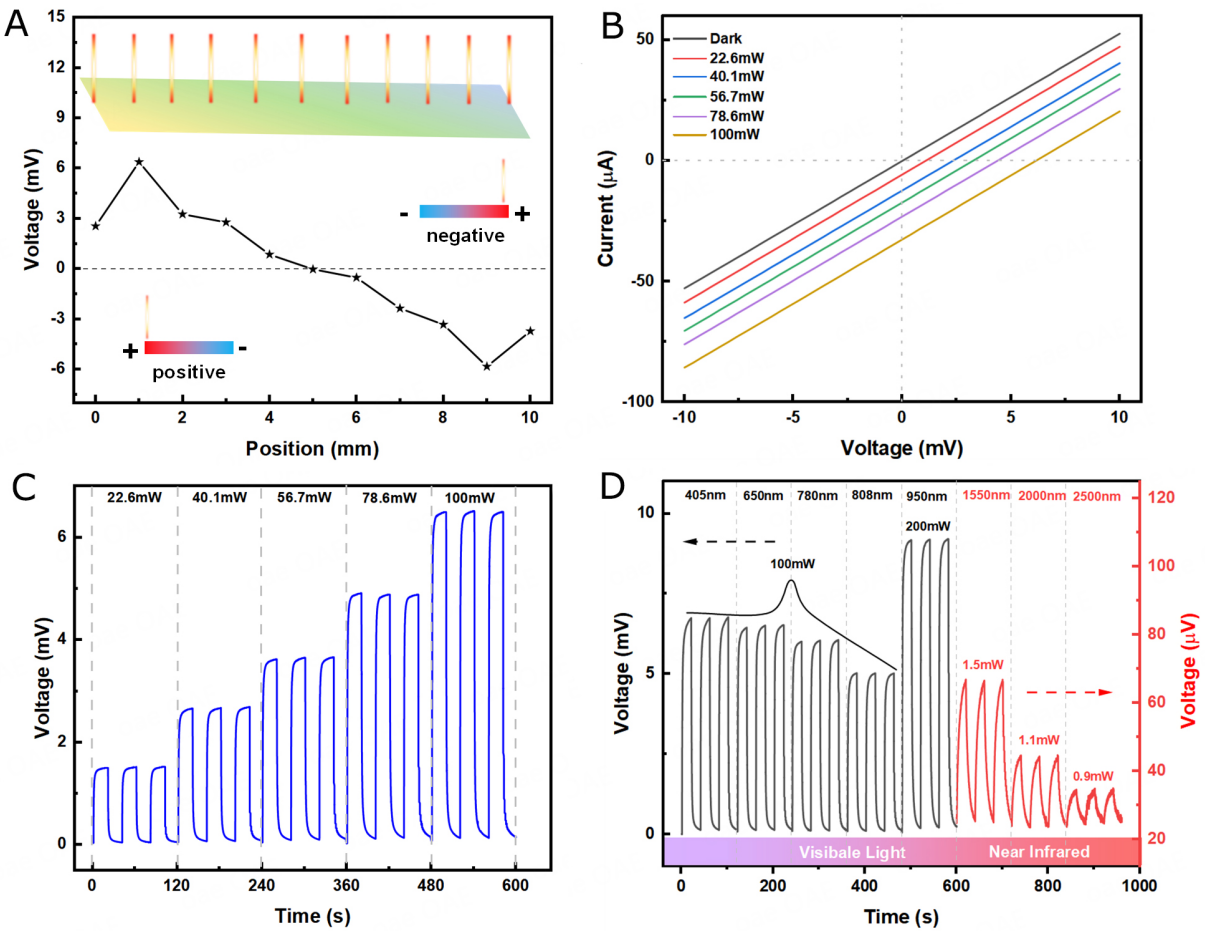

Figure 4. (A) Output voltage versus laser beam position. The wavelength was 650 nm with a power of 100 mW; (B and C) Output voltage and I-V curves at different optical powers. The wavelength was 650 nm; (D) Plots of output voltage versus laser wavelength. The black curve was obtained by testing with a laser light source and the red curve was obtained by combining a monochromator with a xenon light source. I-V: Current-voltage.

thermography and electrical measurements, provide conclusive evidence for the PTE-dominated operation mechanism.

Performance testing of PTE properties

The output voltages at various wavelengths and powers can be derived from Figure 4C and D. The responsivity (R_v) can be calculated using the following Equation (3):

$$R_v = V_{out}/P \tag{3}$$

where V_{out} is the peak voltage and P is the optical power. The relationship between the output voltage and incident optical power is shown in Figure 5A. It can be observed that the output voltage increases with increasing optical power, while the R_v remains constant at 64 mV/W. The detectivity (D^*) reflects the detector's ability to identify weak optical signals. This can be calculated using the following expression. As the device is self-powered, there is no need for external bias, which eliminates the influence of scattering noise and 1/f noise. This means that only Johnson-Nyquist noise remains the main source of noise. Therefore, the noise spectral density (NSD) can be calculated by Equation (4)[19]:

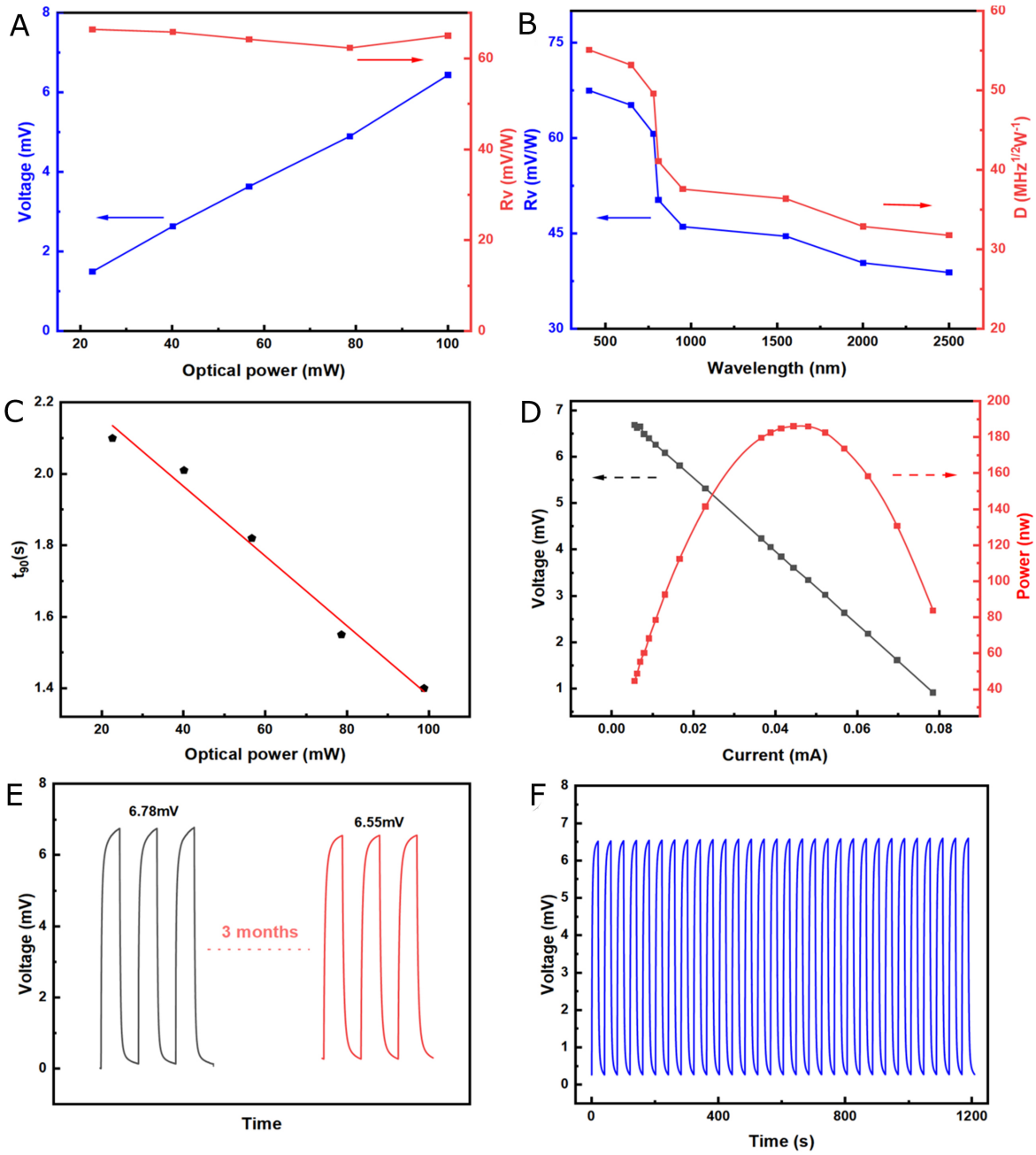

Figure 5. (A) Dependence of photovoltage and R_v on the laser power; (B) Plots of R_v and D as a function of incident wavelength; (C) The functional relationship between t_{90} and optical power; (D) The relationship between the output voltage and current and power. The wavelength was 650 nm with a power of 100 mW; (E and F) Output voltage and stability test results after three months. The wavelength was 405 nm with a power of 100 mW. R_v: Responsivity.

$$NSD \approx NSD_{Johnson} = \sqrt{4Rk_BT} \tag{4}$$

where R is the resistance value of 60 Ω. k_B is the Boltzmann constant and T is the temperature. The noise equivalent power (NEP) and D^* can be further calculated as Equations (5) and (6):

$$NEP = NSD/R_v \tag{5}$$

$$D^* = 1/NEP = R_v/NSD \tag{6}$$

Figure 5B illustrates that both the PTE R_v and D^* decrease with increasing wavelength. This trend arises from the strong reliance of the PTE effect on the interaction between light and matter at the surface, with this interaction weakening as photon energy decreases with increasing wavelength. At a wavelength of 405 nm, the peak values for R_v and D^* are 67.5 mV/W and 55.1 $MHz^{1/2}W^{-1}$, respectively. Moreover, t_{90}, representing the time for the device to achieve 10%-90% of V_{out}, serves as a metric for evaluating the device's response rate, as shown in Figure 5C. This figure indicates an inverse relationship between the response time of PTE and the power of the 650 nm light source. As the optical power increases, the number of incident photons per unit time also increases, leading to a significant increase in the rate of photogenerated carrier production in the material. More carriers can be collected more quickly by the detector's electrodes, which reduces the delay time from light incidence to electrical signal generation[25]. At 100 mW power, t_{90} is 1.4 s. Subsequently, Figure 5D demonstrates the output voltage and the relationship between power and voltage for a 650 nm laser light source irradiated with 100 mW power, with 0.5 wt% APM in series with an adjustable resistor box. The output voltage varies inversely with the current. Maximum power output from the PTE detector occurs when the external resistance of the load matches the internal resistance of the device, as described by Equation (7):

$$P = U^2/R \tag{7}$$

where U is the output voltage and R is the load resistance. Therefore, the relationship between output power and load resistance was established. The PTE detector can produce a maximum output power of 186.1 nW when the load resistance is 60 Ω. Table 1 summarizes a comparison of device performance between other representative detectors and the 0.5 wt% APM detector prepared in this study. The prepared detector demonstrates competitive detection performance and output power properties.

In addition to the output performance of PTE, stability and reliability are other important indicators that determine whether the device can be applied in real and complex working environments. To evaluate the environmental stability of the PTE detector, output voltage tests were repeated using a 400 nm, 100 mW light source after a three-month interval. The device was left exposed to air without encapsulation treatment during this period. As depicted in Figure 5E and F, the voltage only experienced a 3.4% decrease compared to the initial output voltage after three months, demonstrating high stability. Despite the lack of encapsulation, the curve maintained reproducible characteristics and fast response speed over 30 cycles. Thus, these findings suggest that the 0.5 wt% APM utilized in the preparation process offers a wide range of applications in the development of high-performance room-temperature broad-spectrum detectors.

CONCLUSIONS

In summary, the TE properties of MWCNT composite films with varying contents under Ag_2Se/PVP were investigated for their potential applications in PTE conversion. Among the composite films tested, the one containing 0.5 wt% MWCNTs exhibited the most promising PTE performance under light conditions. At a wavelength of 405 nm and with a 100 mW laser, this film achieved remarkable figures of merit with a R_v of 67.5 mV/W and D^* of 55.1 $MHz^{1/2}W^{-1}$. Similarly, under a 650 nm, 100 mW laser, the device demonstrated a rapid response time of 1.4 s and an impressive output power of 186.1 nW. Moreover, the device exhibited exceptional environmental stability and reliability, with only a 3.4% decrease in voltage after three months compared to the initial output voltage, indicating minimal degradation. The reproducible characteristics

Table 1. Comparison of our work with the reported response range, single-leg output voltage, response time, and output power of PTE detector devices with different types

Index	Composite	Spectral range	Light source mode	The number of legs	Output voltage of each leg/mV	Response time/s	Output power of each leg/nW	Ref.
1	PEDOT:PSS/Te NWs	-	xenon lamp	18	0.806	2.13×10^3 s	0.0261	[44]
2	ZnO	365 nm	227.4 mW/cm^2	1	1.300	~100 s	0.780	[45]
3	MoS_2/PU-PEDOT:PSS/Te NWs	808 nm	2,625 mW/cm^2	1	1.200	50 s	0.261	[7]
4	Au/PEDOT/Ag_2Se	-	100 mW/cm^2 (AM1.5G)	12	2.830	17 s	12.2	[46]
5	PPy/Ag_2Se	808 nm	100 mW	1	3.750	18 s	750	[25]
6	PPy/HCNTs	808 nm	400 mW/cm^2	1	0.720	60 s	0.0446	[12]
7	PEDOT:PSS/HCNTs	808 nm	166.01 mW/cm^2	3	0.372	~7.8 s	0.85	[34]
8	PEDOT	808 nm	60 mW	1	0.75	~100 s	-	[47]
9	SnSe	405-1,550 nm	30 mW (523 nm)	1	4.32	3 s	21.8	[10]
10	PEDOT:PSS/PPy	400-1,000 nm	14.95 mW/cm^2	7	0.32	~30 s	0.1	[48]
11	Ag_2Se/PVP/0.5 wt% MWCNTs	405-2,500 nm	100 mW (650 nm)	1	6.45	1.4 s	186.1	This work

PTE: Photothermoelectric; PPy: polypyrrole; PVP: polyvinyl pyrrolidone; MWCNTs: multi-walled carbon nanotubes.

and fast response speed observed over 30 cycles underscored the device's high stability. This study successfully fabricated efficient PTE detectors using screen printing technology, highlighting its potential for flexible PTE device fabrication. These findings provide valuable insights for further optimizing material properties and serve as a significant reference for the development of flexible PTE detector devices in the future.

DECLARATIONS

Authors' contributions

Conceptualization, Investigation, Methodology, Data curation, Writing-Original draft: Shi, W.P.; Chen, Y.; Liu, D.

Conceptualization, Investigation, Software: Guo, R.; Liu, D.; Tian, G.L.

Supervision, Project administration, Writing-review & editing: Xue, C.Y.; Cui, D.F.

Funding acquisition: Liu, D.; Wang, Y.H.; Chen, Y.; Cui, D.F.; Xue, C.Y.

Validation, Software: Shi, W.P.; Guo, R.; Xue, C.Y.; Tian, G.L.; Liu, D.; Cui, D.F.; Wang, Y.H.

Availability of data and materials

The detailed materials and methods in the experiment are presented in the Supplementary Materials. Other raw data that support the findings are available from the corresponding author upon reasonable request.

Financial support and sponsorship

This research was financially supported by the National Natural Science Foundation of China (62371425, 62205308, 62201521, 62304210), the Research Project Supported by Shanxi Scholarship Council of China (2022-144), the Subject Reserve Young Talent Support Program of North University of China, the Fundamental Research Program of Shanxi Province (202103021223202, 202303021222106), the special fund for Science and Technology Innovation Teams of Shanxi Province (202304051001030), and the National Key Research and Development Program of China (2022YFB3205300).

Conflicts of interest

All authors declared that there are no conflicts of interest.

Ethical approval and consent to participate

Not applicable.

Consent for publication

Not applicable.

Copyright

© The Author(s) 2025.

REFERENCES

1. Wang, B. X.; Xu, C.; Duan, G.; Xu, W.; Pi, F. Review of broadband metamaterial absorbers: from principles, design strategies, and tunable properties to functional applications. *Adv. Funct. Materials.* **2023**, *33*, 2213818. DOI
2. Chen, J.; Ouyang, W.; Yang, W.; He, J. H.; Fang, X. Recent progress of heterojunction ultraviolet photodetectors: materials, integrations, and applications. *Adv. Funct. Materials.* **2020**, *30*, 1909909. DOI
3. Wang, H. P.; Li, S.; Liu, X.; Shi, Z.; Fang, X.; He, J. H. Low-dimensional metal halide perovskite photodetectors. *Adv. Mater.* **2021**, *33*, e2003309. DOI PubMed
4. Ely, F.; Vieira, K. O.; Reyes-Banda, M. G.; Quevedo-Lopez, M. Broadband photodetectors from silane-passivated $CsPbBr_3$ nanocrystals by ultrasound-mediated synthesis. *Nanoscale* **2024**, *16*, 10833-40. DOI PubMed
5. Chen, B.; Xu, J.; Shi, S.; Kong, L.; Zhang, X.; Li, L. UV-Vis-NIR broadband self-powered $CuInS_2/SnO_2$ photodetectors and the application in encrypted optical communication. *ACS. Appl. Mater. Interfaces.* **2024**, *16*, 28917-27. DOI PubMed
6. Zhang, Y.; Li, H.; Wang, L.; et al. Photothermoelectric and photovoltaic effects both present in MoS_2. *Sci. Rep.* **2015**, *5*, 7938. DOI PubMed PMC
7. He, M.; Lin, Y. J.; Chiu, C. M.; et al. A flexible photo-thermoelectric nanogenerator based on MoS_2/PU photothermal layer for infrared light harvesting. *Nano. Energy.* **2018**, *49*, 588-95. DOI
8. Lu, X.; Jiang, P.; Bao, X. Phonon-enhanced photothermoelectric effect in $SrTiO_3$ ultra-broadband photodetector. *Nat. Commun.* **2019**, *10*, 138. DOI PubMed PMC
9. Lu, X.; Sun, L.; Jiang, P.; Bao, X. Progress of photodetectors based on the photothermoelectric effect. *Adv. Mater.* **2019**, *31*, e1902044. DOI PubMed
10. Zhong, Y.; Zhang, L.; Linseis, V.; et al. High-quality textured SnSe thin films for self-powered, rapid-response photothermoelectric application. *Nano. Energy.* **2020**, *72*, 104742. DOI
11. Cheng, P.; Ziegler, M.; Ripka, V.; et al. Black silver: three-dimensional Ag hybrid plasmonic nanostructures with strong photon coupling for scalable photothermoelectric power generation. *ACS. Appl. Mater. Interfaces.* **2022**, *14*, 16894-900. DOI PubMed
12. Jin, X. Z.; Qi, X. D.; Wang, Y.; et al. Polypyrrole/helical carbon nanotube composite with marvelous photothermoelectric performance for longevous and intelligent internet of things application. *ACS. Appl. Mater. Interfaces.* **2021**, *13*, 8808-22. DOI PubMed
13. Zhang, Y.; Fan, Z.; Wen, N.; et al. Novel wearable pyrothermoelectric hybrid generator for solar energy harvesting. *ACS. Appl. Mater. Interfaces.* **2022**, *14*, 17330-9. DOI PubMed
14. Zhang, M.; Liu, Y.; Guo, F.; et al. High-performance flexible broadband photothermoelectric photodetectors based on tellurium films. *ACS. Appl. Mater. Interfaces.* **2024**, *16*, 6152-61. DOI PubMed
15. Niu, Y.; Wang, Y.; Wu, W.; et al. Ultrabroadband, fast, and flexible photodetector based on $HfTe_5$ crystal. *Adv. Opt. Mater.* **2020**, *8*, 2000833. DOI
16. Zhang, T.; Ren, Z.; Guo, S.; Zhang, G.; Wang, S.; Qiao, S. Broadband self-powered CdS ETL-based $MAPbI_3$ heterojunction photodetector induced by a photovoltaic-pyroelectric-thermoelectric effect. *ACS. Appl. Mater. Interfaces.* **2023**, *15*, 44444-55. DOI PubMed
17. Ma, J.; Chen, M.; Qiao, S.; Chang, J.; Fu, G.; Wang, S. Photovoltaic-pyroelectric coupled effect in Ag_2Se/Si heterojunction for broadband, ultrafast, self-powered, position-sensitive detectors. *ACS. Photonics.* **2022**, *9*, 2160-9. DOI
18. Wu, W.; Wang, Y.; Niu, Y.; et al. Thermal localization enhanced fast photothermoelectric response in a quasi-one-dimensional flexible NbS_3 photodetector. *ACS. Appl. Mater. Interfaces.* **2020**, *12*, 14165-73. DOI PubMed
19. Wang, R.; He, Z.; Wang, J. L.; Liu, J. Y.; Liu, J. W.; Yu, S. H. Manipulating nanowire structures for an enhanced broad-band flexible photothermoelectric photodetector. *Nano. Lett.* **2022**, *22*, 5929-35. DOI PubMed
20. Sahu, S.; Panda, J.; Haider, G.; Frank, O.; Kalbáč, M.; Velický, M. Self-biased high-responsivity photodetector based on a Bi_2SeTe_2 topological insulator. *ACS. Appl. Electron. Mater.* **2023**, *5*, 6697-703. DOI
21. Zhang, M.; Ban, D.; Xu, C.; Yeow, J. T. W. Large-area and broadband thermoelectric infrared detection in a carbon nanotube black-body absorber. *ACS. Nano.* **2019**, *13*, 13285-92. DOI PubMed

22. Wang, Y.; Niu, Y.; Chen, M.; et al. Ultrabroadband, sensitive, and fast photodetection with needle-like $EuBiSe_3$ single crystal. *ACS. Photonics.* **2019**, *6*, 895-903. DOI
23. Li, G.; Yin, S.; Tan, C.; et al. Fast photothermoelectric response in CVD-grown $PdSe_2$ photodetectors with in-plane anisotropy. *Adv. Funct. Mater.* **2021**, *31*, 2104787. DOI
24. Perez-Taborda, J. A.; Caballero-Calero, O.; Vera-Londono, L.; Briones, F.; Martin-Gonzalez, M. High thermoelectric *zT* in n-type silver selenide films at room temperature. *Adv. Energy. Mater.* **2018**, *8*, 1702024. DOI
25. Yang, Z. Y.; Jin, X. Z.; Huang, C. H.; Lei, Y. Z.; Wang, Y. Constructing A/B-side heterogeneous asynchronous structure with Ag_2Se layers and bushy-like PPy toward high-performance flexible photo-thermoelectric generators. *ACS. Appl. Mater. Interfaces.* **2022**, *14*, 33370-82. DOI PubMed
26. Wen, D. L.; Liu, X.; Bao, J. F.; et al. Flexible hybrid photo-thermoelectric generator based on single thermoelectric effect for simultaneously harvesting thermal and radiation energies. *ACS. Appl. Mater. Interfaces.* **2021**, *13*, 21401-10. DOI PubMed
27. Soni, S. K.; Thomas, B.; Thomas, S. B.; Tile, P. S.; Sakharwade, S. G. Carbon nanotubes as exceptional nanofillers in polymer and polymer/fiber nanocomposites: an extensive review. *Mater. Today. Commun.* **2023**, *37*, 107358. DOI
28. Wu, N.; Liu, Y.; Wang, S.; Xing, Z. Thermal rectification across an asymmetric layer carbon nanotube van der Waals heterostructure. *ACS. Appl. Mater. Interfaces.* **2024**, *16*, 9155-68. DOI PubMed
29. Yang, K.; Wu, Y.; Wang, W.; et al. Stretchable, flexible fabric heater based on carbon nanotubes and water polyurethane nanocomposites by wet spinning process. *Nanotechnology* **2024**, *35*, 125706. DOI PubMed
30. Naik, B. R.; Arya, N.; Balakrishnan, V. Paper based flexible MoS_2-CNT hybrid memristors. *Nanotechnology* **2024**, *35*, 215201. DOI PubMed
31. Kang, J.; Bai, C.; Liu, S.; Jia, Y. Light-induced nontethered rolling of liquid crystal elastomer and carbon nanotube composite ring. *ACS. Appl. Polym. Mater.* **2024**, *6*, 2709-18. DOI
32. Chen, C.; Chen, Z.; Hu, S.; Zhou, Y.; Huang, Z.; Zhou, H. Significantly enhanced laser trapping and heating of carbon nanotube/carbon fibre hierarchical composites for efficient laser-assisted automated fibre placement. *Compos. Part. A. Appl. Sci. Manuf.* **2024**, *177*, 107965. DOI
33. Cai, Y.; Yu, H.; Cheng, L.; et al. Structure design, surface modification, and application of CNT microwave-absorbing composites. *Adv. Sustain. Syst.* **2023**, *7*, 2300272. DOI
34. Jin, X. Z.; Li, H.; Wang, Y.; et al. Ultraflexible PEDOT:PSS/Helical carbon nanotubes film for all-in-one photothermoelectric conversion. *ACS. Appl. Mater. Interfaces.* **2022**, *14*, 27083-95. DOI PubMed
35. Wang, J.; Xie, Z.; Liu, J. A.; Zhou, R.; Lu, G.; Yeow, J. T. W. System design of large-area vertical photothermoelectric detectors based on carbon nanotube forests with MXene electrodes. *Nanoscale. Adv.* **2023**, *5*, 1133-40. DOI PubMed PMC
36. Nunna, R.; Qiu, P.; Yin, M.; et al. Ultrahigh thermoelectric performance in Cu_2Se-based hybrid materials with highly dispersed molecular CNTs. *Energy. Environ. Sci.* **2017**, *10*, 1928-35. DOI
37. Archana, C.; Harish, S.; Abinaya, R.; Archana, J.; Navaneethan, M. Interface modified MoS_2/CNT with enhanced power factor via energy filtering effect for flexible thermoelectric applications. *Sens. Actuators. A. Phys.* **2022**, *348*, 113938. DOI
38. Taborowska, P.; Wasiak, T.; Sahlman, M.; Lundström, M.; Janas, D. Carbon nanotube-based thermoelectric modules enhanced by ZnO nanowires. *Materials* **2022**, *15*, 1924. DOI PubMed PMC
39. Hu, Q. X.; Liu, W. D.; Zhang, L.; et al. SWCNTs/Ag_2Se film with superior bending resistance and enhanced thermoelectric performance via in situ compositing. *Chem. Eng. J.* **2023**, *457*, 141024. DOI
40. Santhosh, R.; Abinaya, R.; Ponnusamy, S.; Ikeda, H.; Navaneethan, M. Interface scattering induced low thermal conductivity in Ag_2Se/MWCNT for enhanced thermoelectric application. *Diam. Relat. Mater.* **2023**, *140*, 110344. DOI
41. Park, D.; Kim, M.; Kim, J. Preparation and structure dependent thermoelectric properties of flexible N-type nanostructured silver(I) selenide/multi-walled carbon nanotube composite film. *Appl. Surf. Sci.* **2023**, *613*, 156150. DOI
42. Shi, X. L.; Wu, H.; Liu, Q.; et al. $SrTiO_3$-based thermoelectrics: progress and challenges. *Nano. Energy.* **2020**, *78*, 105195. DOI
43. Zhao, Y.; Liu, D.; Yan, Z.; et al. Preparation and characterization of the Ag_2Se flexible films tuned by PVP for wearable thermoelectric generator. *J. Mater. Sci:. Mater. Electron.* **2021**, *32*, 20295-305. DOI
44. Liu, Y.; Lan, X.; Xu, J.; et al. Organic/inorganic hybrid boosting energy harvesting based on the photothermoelectric effect. *ACS. Appl. Mater. Interfaces.* **2021**, *13*, 43155-62. DOI PubMed
45. Zhang, K.; Ouyang, B.; Wang, Y.; Xia, Y.; Yang, Y. Coupling enhancement of photo-thermoelectric conversion in a lateral ZnO nanowire array. *ACS. Appl. Energy. Mater.* **2019**, *2*, 7647-54. DOI
46. Xin, C.; Hu, Z.; Fang, Z.; et al. Flexible and wearable plasmonic-enabled organic/inorganic hybrid photothermoelectric generators. *Mater. Today. Energy.* **2021**, *22*, 100859. DOI
47. Kim, B.; Han, M.; Kim, E. Photothermally powered conductive films for absorber-free solar thermoelectric harvesting. *J. Mater. Chem. A.* **2019**, *7*, 2066-74. DOI
48. Zhang, X.; Li, T. T.; Ren, H. T.; et al. Dual-shell photothermoelectric textile based on a PPy photothermal layer for solar thermal energy harvesting. *ACS. Appl. Mater. Interfaces.* **2020**, *12*, 55072-82. DOI PubMed